JOURNAL OF THE ROYAL SOCIETY Interface

rsif.royalsocietypublishing.org

Research

Cite this article: Gao J, Du P, O'Grady G, Archer R, Farrugia G, Gibbons SJ, Cheng LK. 2013 Numerical metrics for automated quantification of interstitial cell of Cajal network structural properties. J R Soc Interface 10: 20130421.
http://dx.doi.org/10.1098/rsif.2013.0421

Received: 9 May 2013
Accepted: 6 June 2013

Subject Areas:
bioengineering, computational biology

Keywords:
confocal microscopy, maturation, post-natal, pruning, remodelling

Author for correspondence:
Leo K. Cheng
e-mail: l.cheng@auckland.ac.nz

Numerical metrics for automated quantification of interstitial cell of Cajal network structural properties

Jerry Gao[1], Peng Du[1], Greg O'Grady[1,2], Rosalind Archer[3], Gianrico Farrugia[4], Simon J. Gibbons[4] and Leo K. Cheng[1,5]

[1]Auckland Bioengineering Institute, [2]Department of Surgery, and [3]Department of Engineering Science, The University of Auckland, Private Bag 92019, Auckland 1142, New Zealand
[4]Enteric Neuroscience Program, Division of Gastroenterology and Hepatology, Mayo Clinic College of Medicine, 200 First Street SW, Rochester, MN 55905, USA
[5]Department of Surgery, Vanderbilt University, Nashville, TN 37240, USA

Depletion of interstitial cells of Cajal (ICC) networks is known to occur in several gastrointestinal motility disorders. Although confocal microscopy can effectively image and visualize the spatial distribution of ICC networks, current descriptors of ICC depletion are limited to cell numbers and volume computations. Spatial changes in ICC network structural properties have not been quantified. Given that ICC generate electrical signals, the organization of a network may also affect physiology. In this study, six numerical metrics were formulated to automatically determine complex ICC network structural properties from confocal images: *density*, *thickness*, *hole size*, *contact ratio*, *connectivity* and *anisotropy*. These metrics were validated and applied in proof-of-concept studies to quantitatively determine jejunal ICC network changes in mouse models with decreased ($5\text{-}HT_{2B}$ receptor knockout (KO)) and normal (*Ano1* KO) ICC numbers, and during post-natal network maturation. Results revealed a novel remodelling phenomenon occurring during ICC depletion, namely a spatial rearrangement of ICC and the preferential longitudinal alignment. In the post-natal networks, an apparent pruning of the ICC network was demonstrated. The metrics developed here enabled the first detailed quantitative analyses of structural changes that may occur in ICC networks during depletion and development.

1. Introduction

Gastrointestinal (GI) motility, the contractile activity of GI organs required for digestion and transportation of contents along the GI tract, is facilitated by specialized cells called interstitial cells of Cajal (ICC) [1]. ICC exist throughout the muscularis propria of the GI tract and are classified into several populations according to their location [2]. Different populations of ICC also have different functional roles [3]. A primary role of ICC, particularly those within the region of the myenteric plexus (ICC-MP) between the longitudinal and circular smooth muscle layers in the small intestine, is that they act as the primary pacemaker cells responsible for generating and regulating an omnipresent underlying electrical oscillation, termed 'slow waves', that coordinate motility [4,5]. Additional roles ICC are known to play include mediating neurotransmission to smooth muscle cells (SMC) [6], establishing membrane potential gradients in the tissue wall [7] and responding to stretch [8,9].

ICC loss and injury is now a major research focus as it is recognized as a hallmark of several GI motility disorders [10], including gastroparesis [11,12], slow transit constipation [13,14] and intestinal pseudo-obstruction [15,16]. In addition, progressive depletion of ICC is known to occur as part of normal ageing [17].

Since the discovery of ICC-specific immunohistochemical stains, confocal microscopy has been an effective tool for imaging and visualizing the spatial

distribution of ICC throughout the muscularis propria [2,18]. Although the complex network structures formed by ICC can be accurately imaged, current descriptors of ICC loss only involve simple cell (nuclei) counts and volume computations [17,19], and no attempts are currently made to quantify spatial changes that may be occurring in the structural properties of ICC networks. Accurately defining the structural characteristics of ICC networks would allow investigators to explicitly contrast and compare aspects of ICC organization in a consistent, unbiased manner. In addition, the major network structural properties that potentially influence network function and dysfunction could be defined and investigated as, given that ICC generate electrical signals, the organization of a network may also affect physiology.

To advance this problem, this paper presents a set of six numerical metrics to automatically quantify structural properties of confocal ICC network images. These metrics were applied in proof-of-concept studies to quantitatively determine structural changes in ICC networks from *5-HT*$_{2B}$ receptor and *Ano1* knockout (KO) animal models, as well as the changes that occur during network maturation of neonatal animals.

2. Material and methods

2.1. Formulation of numerical metrics

The two-dimensional formulation of the six metrics: density, thickness, hole size, contact ratio, connectivity and anisotropy are described in detail below (§§2.1.1–2.1.6). Two of the six metrics (density and connectivity) were described in a preliminary form in an earlier report by Gao *et al.* [20]. The metrics were inspired by and partly adapted from existing methods of quantifying structure from alternative fields [21,22]. The metrics were initially chosen to quantify ICC network properties that may influence electrical behaviour.

An ICC network image from a *5-HT*$_{2B}$ receptor KO jejunal ICC-MP dataset [19] was used as an example network to illustrate the developed metrics (figures 1*a* and 2*b*). See §2.2.1 for the detailed description of the example network image.

2.1.1. Density

The density metric (ρ) calculates the relative volume of the tissue occupied by ICC (figure 1*b*). This metric is dimensionless and ranges from 0 to 1, with 0 indicating that no ICC were present and 1 indicating that only ICC were present. The density metric was defined as

$$\rho = \frac{N_{\mathrm{ICC}}}{N_{\mathrm{Total}}}, \tag{2.1}$$

where N_{ICC} and N_{Total} are the number of pixels representing ICC and the total number of pixels in the image, respectively.

2.1.2. Thickness

The thickness metric (t) measures the representative width of the ICC network processes and cell bodies (figure 1*c*). This metric, measured in μm, was calculated as a weighted average of the process and cell body widths over the entire ICC network. In computing this metric, the Euclidean distance transform of the ICC network image was first calculated. This returned a distance map of distance from each ICC pixel to the nearest non-ICC pixel (figure 1*i*). The ICC network can be approximated by circles centred on the points of the regional maxima of the distance map, with radii of the regional maximum distances (figure 1*j*). Therefore, the regional maximum values of the distance transform signify the 'radii' of the processes and cell bodies. The thickness metric was then calculated as a scaled weighted sum of these individual thickness radii:

$$t = 2r\sum_{i=1}^{n} tw_i tr_i, \tag{2.2}$$

where r is the resolution of the image in μm, n is the number of regional maxima in the distance map, tr_i is the ith regional maximum value or thickness radius in the distance map and tw_i is the thickness weight applied to tr_i. As the thickness radius only reflected half the width, a scaling factor of 2 was included.

The thickness weights were defined as

$$tw_i = \frac{tr_i^2}{\sum_{i=1}^{n} tr_i^2}. \tag{2.3}$$

The thickness weights were derived as the proportion of total ICC area represented by the individual thickness radii. Visualizing the ICC network image as the circles centred on the regional maxima, the area contributed by the ith regional maxima is πtr_i^2, and the total area of ICC is approximately the sum of the individual circles, $\sum_{i=1}^{n} \pi tr_i^2$. The ratio of these expressions reduce to the above definition (equation (2.3)).

Substituting equation (2.3) into equation (2.2) gave the simplified thickness metric formulation:

$$t = 2r\frac{\sum_{i=1}^{n} tr_i^3}{\sum_{i=1}^{n} tr_i^2}. \tag{2.4}$$

2.1.3. Hole size

The hole size metric (h) measures the representative radius of the non-ICC regions in the ICC network (figure 1*d*). This metric, measured in μm, was calculated as a weighted average of the individual radii of all the non-ICC region holes within the ICC network. The calculation process of this metric was identical to that of the thickness metric, but the Euclidean distance transform computed was that of the non-ICC regions. That is, the distance map in the hole size metric returned the distance from each non-ICC pixel to the nearest ICC pixel (figure 1*k*). Therefore, the hole size metric was defined as

$$h = r\frac{\sum_{i=1}^{n} hr_i^3}{\sum_{i=1}^{n} hr_i^2}, \tag{2.5}$$

where r is the resolution of the image in μm, n is the number of regional maxima in the distance map and hr_i is the ith regional maximum value or hole radius in the distance map.

2.1.4. Contact ratio

The contact ratio metric (ϕ) calculates the proportion of ICC pixels in contact with (i.e. directly neighbouring) non-ICC pixels (figure 1*e*). This metric is measured in $\mu\mathrm{m}^{-1}$, and in two dimensions, is equivalent to the perimeter to area ratio of the ICC network. The contact ratio metric was defined as

$$\phi = \frac{1}{r}\frac{N_{\mathrm{BICC}}}{N_{\mathrm{ICC}}}, \tag{2.6}$$

where r is the resolution of the image in μm, N_{BICC} is the number of border ICC pixels (i.e. ICC pixels directly neighbouring non-ICC pixels) and N_{ICC} is the total number of ICC pixels. In the actual computation of this metric, the pixels along the edges of the image were discarded as the border ICC pixels could not be differentiated with certainty.

2.1.5. Connectivity

The connectivity metric (c) indicates how connected (or disconnected) the ICC network is. This metric, measured in μm, was computed as the ratio of tissue area to disconnection or 'gap' severity of the ICC network (figure 1*f*). The ICC network may be formed by more than one group of interconnected ICC pixels,

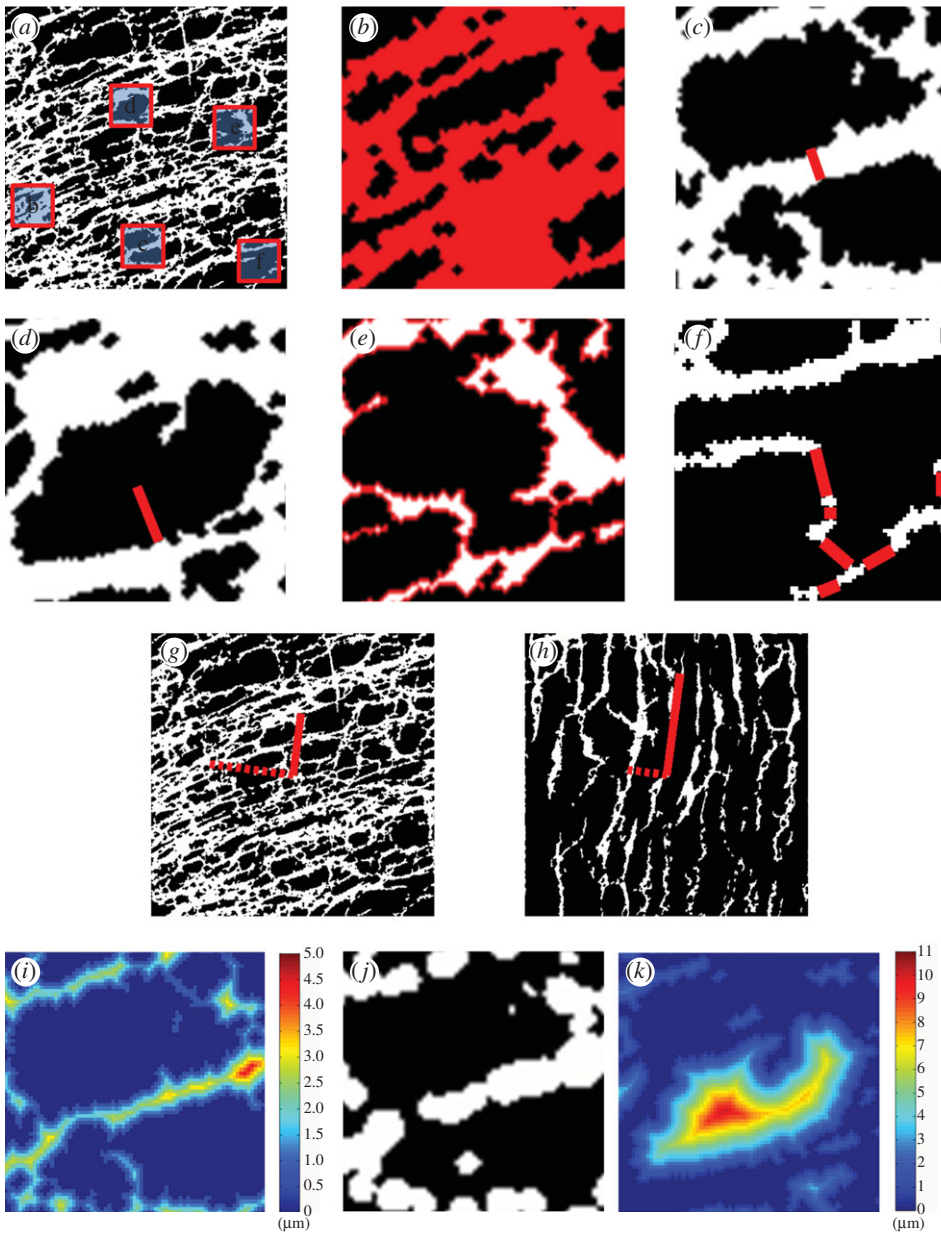

Figure 1. Illustration of the six numerical metrics on a sample ICC network (*a*) with specific regions magnified in (*b*–*f*). (*b*) Density metric: the proportion of the image that was populated by ICC (red) was calculated. (*c*) Thickness metric: the representative thickness of the ICC bodies/processes (as indicated by length of red line) was computed. (*d*) Hole size metric: the representative radius of the non-ICC regions (as indicated by length of red line) was computed. (*e*) Contact ratio metric: the ratio of ICC that was immediately neighbouring non-ICC (red) to total ICC (white and red) was calculated. (*f*) Example ICC network overlaid with red lines that connect the ICC islands together with shortest summed distance. These connections denote the 'gaps' or lack of connectivity of the network. Note that as this is a magnified view of the original network in (*a*), the two seemingly separate islands at the top of the current field of view are actually connected, and hence no connection was drawn to the top island. (*g*) Example ICC network with vectors in the circular (solid) and longitudinal (dashed) directions scaled so the magnitudes were proportional to the respective alignment strengths. (*h*) Corresponding ICC-DMP network of the example ICC network with vectors in the circular (solid) and longitudinal (dashed) directions as found using PCA. The vectors were scaled so the magnitudes were proportional to the respective eigenvalues (alignment strengths). (*i*) Euclidian distance transform of the magnified ICC network in (*c*), which was used in computing the thickness metric. (*j*) Approximation of the magnified ICC network in (c), used in computing the thickness metric. This network approximation was constructed by centring circles on the points of the regional maxima of the distance map, with radii of the regional maximum distances. (*k*) Euclidian distance transform of the non-ICC regions within the magnified ICC network in (*d*), which was used in computing the hole size metric. The background (black) of (*a*–*h*) and (*j*) represents non-ICC regions.

and here these individual groups are termed islands. Assuming there are n islands, the $n-1$ connections that join the n islands together with the shortest summed distance, or the minimum spanning tree, can be determined using Prim's algorithm [23]. Starting from an arbitrary island, islands were connected sequentially until all islands were joined. The connectivity metric was then computed as the ratio of image area to the weighted sum of the individual connection distances, and was defined as

$$c = r\frac{N_{\text{Total}}}{\sum_{i=1}^{n-1} cw_i cd_i}, \tag{2.7}$$

where r is the resolution of the image in μm, n is the number of ICC islands, N_{Total} is the total number of pixels in the image, cd_i is the ith connection distance and cw_i is the connection weight of cd_i. The weighted distance sum in the denominator reflects the severity of 'gaps' in the network.

The connection weights were defined as

$$cw_i = \frac{N_i}{N_{\text{ICC}}}, \tag{2.8}$$

where N_i is the number of pixels in the ith connected island and N_{ICC} is the total number of ICC pixels. The weights were the

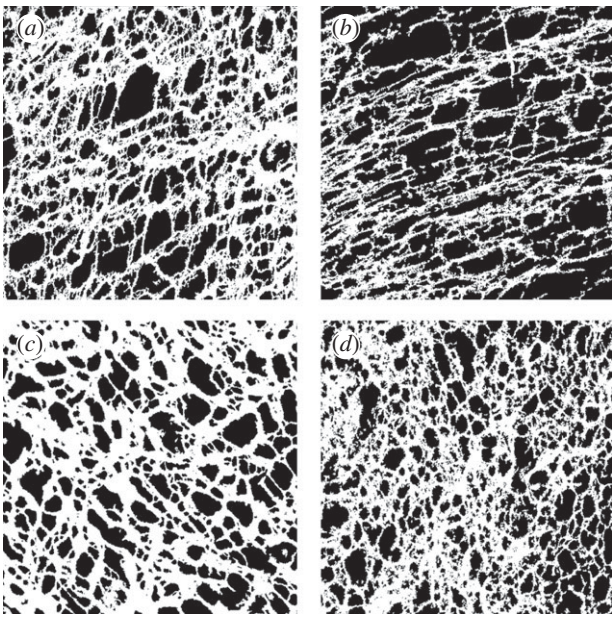

Figure 2. Representative ICC network images for each group of the datasets, as objectively defined by having metric values near the median of the group. Shown are 4-week-old (*a*) WT and (*b*) KO from *5-HT$_{2B}$* receptor dataset, with physical dimensions of 0.318 × 0.318 mm, and 3-day-old (*c*) WT and (*d*) KO from *Ano1* dataset, with physical dimensions of 0.212 × 0.212 mm. The white represents ICC, while the black represents non-ICC regions.

ratios of the added island sizes to the total number of ICC pixels, and hence gauged the size of the added islands. This weighting factor was included as when measuring gap severity, not only are the distances between the islands important, but the relative sizes of the separated islands need to be considered as well. For example, the gap induced by a large island should be considered more severe than that induced by a small island the same distance away. Also for this reason, the arbitrary starting island was selected to be the largest island, so only the smaller islands were considered as 'additions' and the weighted distance sum of the network was not falsely increased.

Combining equations (2.7) and (2.8) gave

$$c = r\frac{N_{\mathrm{ICC}}N_{\mathrm{Total}}}{\sum_{i=1}^{n-1} N_i c d_i}. \tag{2.9}$$

2.1.6. Anisotropy

The anisotropy metric (*a*) reflects the preferential alignment of the ICC network processes in the longitudinal or circular directions of the organ. This metric is dimensionless and ranges from −1 to 1, with a positive value indicating preferential alignment in the longitudinal direction, and a negative value indicating preferential alignment in the circular direction. The magnitude of the metric reflects the strength of the preferential alignment. Several steps were involved in computing this metric:

(1) The power spectral density (P) of the image was calculated.

$$P = |F|^2, \tag{2.10}$$

where F is the two-dimensional Fourier transform of the network image.

(2) The normalized covariance matrix ($\bar{C}$) of P was calculated.

$$\bar{C} = \frac{1}{\bar{\mu}_{00}}\begin{bmatrix} \bar{\mu}_{20} & \bar{\mu}_{11} \\ \bar{\mu}_{11} & \bar{\mu}_{02} \end{bmatrix} \tag{2.11}$$

$\bar{\mu}_{pq}$, the normalized central moments were defined as

$$\bar{\mu}_{pq} = \sum_{i=1}^{w}\sum_{j=1}^{h} \frac{(i-\bar{i})^p (j-\bar{j})^q}{((i-\bar{i})^2 + (j-\bar{j})^2)^{(p+q)/2}} P(i,j) \tag{2.12}$$
$$\text{for} \quad p,q = 0,1,2\ldots,$$

where h and w are the dimensions (height and width) of the image in pixels, $\bar{i}$ and $\bar{j}$ are the x- and y-coordinates of the centroid position of the image, respectively, and $P(i, j)$ is the power spectral density value at position (i, j). The only difference between equation (2.12) and the central moment definition is the division of the normalization term $((i-\bar{i})^2 + (j-\bar{j})^2)^{(p+q)/2}$. When summing over the individual (i, j) positions, the standard central moment scales the further away positions by a larger amount. However, in P, these further away positions correspond to higher spatial frequencies which may in fact be noise. Therefore, all positions were normalized to have equal influence on the final summed value, and only the orientations of the positions were retained.

(3) The alignment strengths in the longitudinal (λ_{L}) and circular (λ_{C}) directions were calculated.

$$\lambda_i = |\bar{C}\bar{V}_i| \quad \text{for } i = \mathrm{L}\,\text{or}\,\mathrm{C}, \tag{2.13}$$

where $\bar{V}_{\mathrm{L}}$ and $\bar{V}_{\mathrm{C}}$ are the normalized vectors in the longitudinal and circular directions, respectively. These unit vectors were projected onto the mapping matrix $\bar{C}$, and the magnitudes of the resultant vectors reflect the strengths of alignment in the respective directions (figure 1*g*).

(4) The anisotropy metric (*a*) was calculated.

$$a = \begin{cases} \sqrt{1 - \dfrac{\lambda_{\mathrm{C}}}{\lambda_{\mathrm{L}}}} & \text{if } \lambda_{\mathrm{L}} \geq \lambda_{\mathrm{C}}, \\ -\sqrt{1 - \dfrac{\lambda_{\mathrm{L}}}{\lambda_{\mathrm{C}}}} & \text{if } \lambda_{\mathrm{L}} < \lambda_{\mathrm{C}}. \end{cases} \tag{2.14}$$

2.2. Interstitial cell of Cajal network imaging data

2.2.1. Imaging datasets

The developed metrics were applied in demonstration studies to analyse jejunal ICC network confocal images. The two principal ICC layers in the murine small intestine are in the MP (ICC-MP) and the deep muscular plexus (ICC-DMP) between the inner thin and outer thick sublayers of the circular muscle [24]. However, as ICC-MP have been identified as the primary pacemakers of slow waves in the small intestine [4], only the network structure of these cells were analysed.

Two-dimensional bitmap images of the Kit-positive ICC structures were obtained as previously described [19,25]. Briefly, intestinal sections were dissected quickly, then flushed with ice-cold calcium-free Hanks balanced salt-solution (Invitrogen, Carlsbad, CA), and immediately pinned onto sylgard lined Petri dishes to mitigate against tissue deformation. All specimens were handled and prepared in exactly the same manner. Confocal image slices were sequentially taken throughout the transmural depth of the muscularis propria in fine steps of 0.2–0.3 µm and were volume-rendered in three dimensions. Bitmaps of the positively labelled structures were then obtained using the Analyze software (AnalyzeDirect, Overland Park, KS) as previously described [26]. Unbiased thresholding algorithms were used to segment the images and determine the volume of the Kit-positive structures, thereby minimizing any human influence in the process. The ICC-MP network was relatively thin in the transmural direction (≈10 µm) and the majority of the network laid in-plane. Therefore, the image segments of the ICC-MP were depth-averaged into two-dimensional images representing the entire ICC-MP network structures.

Imaging data taken from the *5-HT$_{2B}$* receptor and *Ano1* murine datasets were analysed, and the details are as follows:

(1) *5-HT$_{2B}$ receptor dataset*. This dataset contained 23 wild-type (WT) and 23 *5-HT$_{2B}$* serotonin receptor KO jejunal ICC network images from 4-week-old mice (figure 2*a*,*b*). ICC express *5-HT$_{2B}$* receptors, and stimulation with *5-HT* (serotonin) increases ICC proliferation and numbers [27]. It has also been demonstrated that a lack of *5-HT$_{2B}$* receptors decrease ICC proliferation, numbers and network volume [19]. These images were 512×512 pixels, and represented physical dimensions ranging from 0.225×0.225 mm to 0.318×0.318 mm.
(2) *Ano1 dataset*. This dataset consisted of 16 WT and 16 *Ano1* KO jejunal ICC network images from 3-day-old mice (figure 2*c*,*d*). *Ano1* is a Ca^{2+}-activated Cl^- channel expressed by ICC [28], and ICC lacking *Ano1* channels have been shown to have fewer proliferating ICC [29] but normal numbers of adult ICC. These images were 512×512 pixels, and represented physical dimensions of 0.212×0.212 mm.

These imaging data are available in the Physiome Model Repository via http://models.physiomeproject.org/w/jerry.gao/Gao_et_al_2013. It can be seen from the individual images that the standard biological variability of ICC networks is large, and hence numerous network structures were included in each group of the imaging datasets ($n = 23$ or 16).

2.2.2. Orientation of imaging data

The computation of the anisotropy metric (see §2.1.6) required knowledge on the orientation of the ICC network imaging data relative to the longitudinal and circular directions. However, this orientation information was not directly available from the images, so an alternative strategy to determine the imaging data orientation was developed. ICC-DMP processes are aligned in the circumferential direction [24], and hence the imaging data of these cells can be used as a reference to determine the relative orientation of the ICC-MP.

Two-dimensional bitmap images of the ICC-DMP network were obtained in the same way as the ICC-MP networks (see §2.2.1). These imaging data are also available in the Physiome Model Repository via http://models.physiomeproject.org/w/jerry.gao/Gao_et_al_2013. The process of extracting the orientation information from the ICC-DMP imaging data proceeded as follows:

(1) The normalized covariance matrix ($\bar{C}$) (see equation (2.11)) of the ICC-DMP image was computed.
(2) Principal component analysis (PCA) [30] was applied on $\bar{C}$ to find the orthogonal eigenvectors and the corresponding eigenvalues of the matrix.

In two dimensions, generally an eigenvector pair with two corresponding eigenvalues exists. The projection in the circular direction is expected to be the strongest due to the dominant alignment of the ICC-DMP processes, and since the orientations of features in the frequency domain are orthogonal to the original orientations in the spatial domain [22], the eigenvector with larger (i.e. maximum) eigenvalue points in a direction at right angles to the circular direction. Assuming the longitudinal and circular directions are orthogonal, the eigenvector with larger eigenvalue points in the longitudinal direction, while the other eigenvector points in the circular direction (figure 1*h*).

2.2.3. Pre-processing of imaging data

Before computing the metric values of the ICC-MP networks, pre-processing of the images was conducted.

(1) *Joining of small gaps*. Gaps with less than 1 pixel radius were morphologically closed by performing an image dilation followed by erosion using a circular structuring template with radius of 1 pixel. This step avoided islands of ICC being separated by small gaps which may be imaging artefacts, and although the joining of these gaps did not change the networks much visually, the metric values may be significantly affected.
(2) *Removal of small islands*. Islands with less than 4 pixels were removed. These islands had area less than 2×2 pixels, and hence were considered unlikely to be a genuine or significant ICC structure in terms of the network geometry as a whole. Again, the removal of these islands did not introduce obvious visual differences, but the metric values may be considerably influenced.

3. Results

3.1. Quantification of network structural differences

3.1.1. *5-HT$_{2B}$* receptor knockout

The metric values of the WT and KO networks from the *5-HT$_{2B}$* receptor dataset are plotted in figure 3. These data showed that the KO networks had on average a 24 per cent lower density ($p < 0.01$), 34 per cent lower thickness ($p < 0.01$), 63 per cent higher contact ratio ($p < 0.01$) and 96 per cent lower connectivity ($p < 0.01$) than that of the WT networks. The KO networks also had on average a higher anisotropy metric value compared with the WT networks (KO mean: 0.44, WT mean: 0.01; $p < 0.01$), indicating an increased preferential alignment of the ICC network processes in the longitudinal direction in the ICC-depleted dataset. There was no difference between the hole size of the WT and KO networks ($p = 0.15$).

3.1.2. *Ano1* knockout

The metric values of the WT and KO networks from the *Ano1* dataset are plotted in figure 4. There were no differences between the metric values of the WT and KO networks (density: $p = 0.31$; thickness: $p = 0.27$; hole size: $p = 0.59$; contact ratio: $p = 0.81$; connectivity: $p = 0.14$ and anisotropy: $p = 0.65$).

3.1.3. Network maturation

The metric values of the WT networks from the *Ano1* and *5-HT$_{2B}$* receptor datasets were compared to examine ICC network structural changes potentially occurring during post-natal maturation (3-day- and 4-week-old, respectively), and the results are plotted in figure 5. These results demonstrated that the 4-week networks had on average a 38 per cent higher thickness ($p < 0.01$), 45 per cent higher hole size ($p < 0.01$), 37 per cent lower contact ratio ($p < 0.01$) and 3 times higher connectivity ($p = 0.02$) as compared with the 3-day networks. There was no difference in the density ($p = 0.12$) or anisotropy ($p = 0.88$) between the 3-day and 4-week networks.

3.2. Metric relationships

A strong nonlinear relationship between the thickness and contact ratio metrics was observed (figure 6). In general, the thinner the network processes the higher the contact ratio. No other obvious metric relationships were identified.

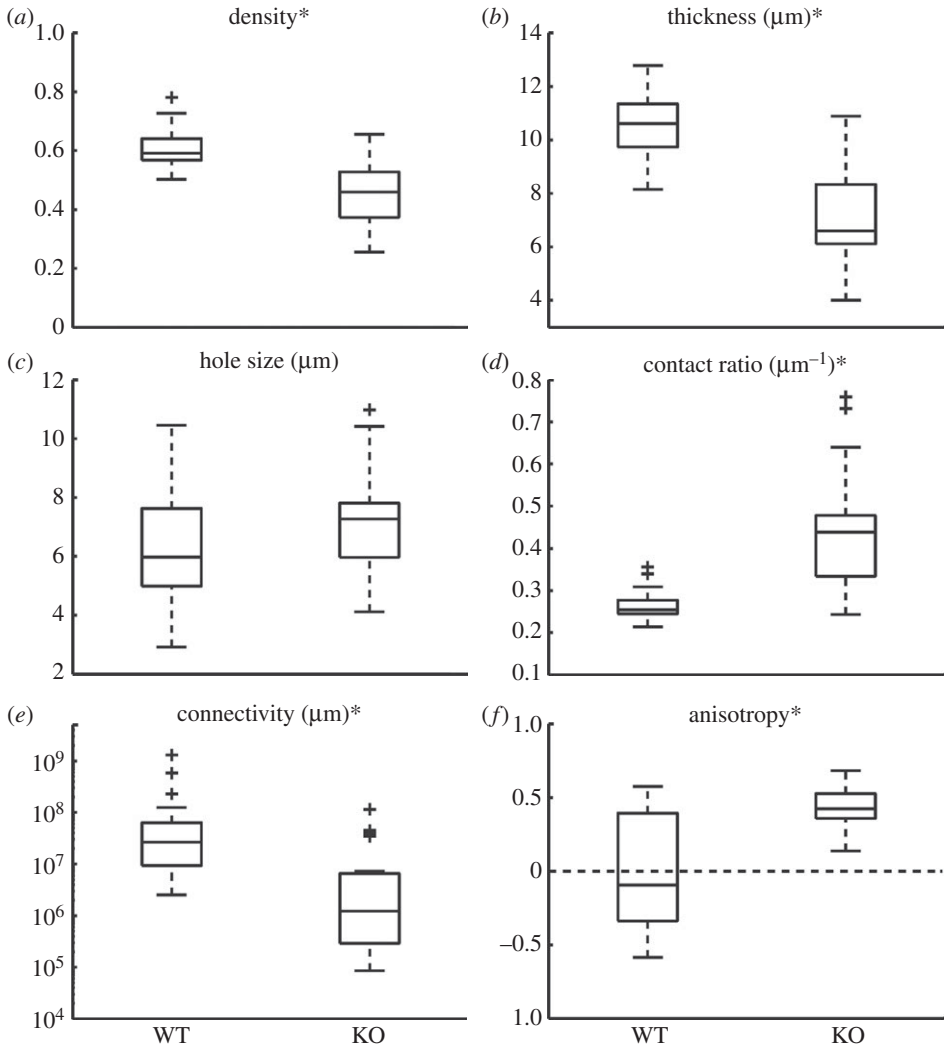

Figure 3. Metric values of ICC networks from *5-HT$_{2B}$* receptor dataset. An asterisk in the figure title indicates a statistically significant difference ($p < 0.05$). A plus symbol in the boxplot resembles an outlier.

4. Discussion

The current quantitative measures of cell counts and volume computations for ICC networks from full-thickness tissue biopsies have identified several clinical conditions involving significant ICC depletion, including gastroparesis [11,12] and diabetes [31]. However, at the same time, there are also patients with significant symptoms but apparently normal ICC numbers [11,12]. This may not only reflect primary pathological involvement of other cell types including macrophages and neurons, but also may reflect changes to ICC networks that affect function not captured by the relatively simplistic measures currently used. This study has presented six metrics for defining the structural properties of ICC networks in confocal images. These metrics enable detailed quantifications of the density, thickness, spacing, contact, connectivity and alignment of ICC populations. To show their validity and utility, the metrics were applied in demonstration studies to reveal novel insights into structural changes occurring during ICC depletion and maturation.

Each of the developed ICC structural metrics was formulated for potential physiological relevance. As this study examined ICC-MP network structures, potential physiological relevance was considered in the context of the pacemaker activity generated by ICC-MP (table 1). The definitive functional effects of these structural metrics can be better clarified once further structure–function studies using these developed metrics are conducted.

In the demonstration studies, ICC networks were found to be depleted and structurally altered in *5-HT$_{2B}$* KO mice but not in *Ano1* KO mice. These data support and extend the previous analyses on these models using cell counts and volume computations [19,29], with more detailed structural and statistical evidence. Although *Ano1* regulates ICC proliferation [29], alternative mechanisms of proliferation such as Kit [35] and serotonin [19,27] may compensate in the *Ano1* KO model, resulting in structurally normal ICC networks.

During ICC depletion in the *5-HT$_{2B}$* receptor KO mouse model, the network density decreased, the ICC processes thinned and the network became less connected. However, the increased contact ratio in the KO networks may be due to the decreased thickness in contrast to a structural adaptation. The data also revealed, for the first time, that a potential remodelling phenomenon may occur in ICC-depleted networks. Despite the fact that the ICC processes thinned, the hole size metric value of the KO networks did not increase, suggesting a spatial rearrangement of ICC to maintain a consistent spread over adjacent SMC. Spatial remodelling in response to the SMC distribution is feasible, because SMC are primarily responsible for the production of stem cell factor, which is the most important promoter of ICC regeneration and survival [36]. Such a rearrangement

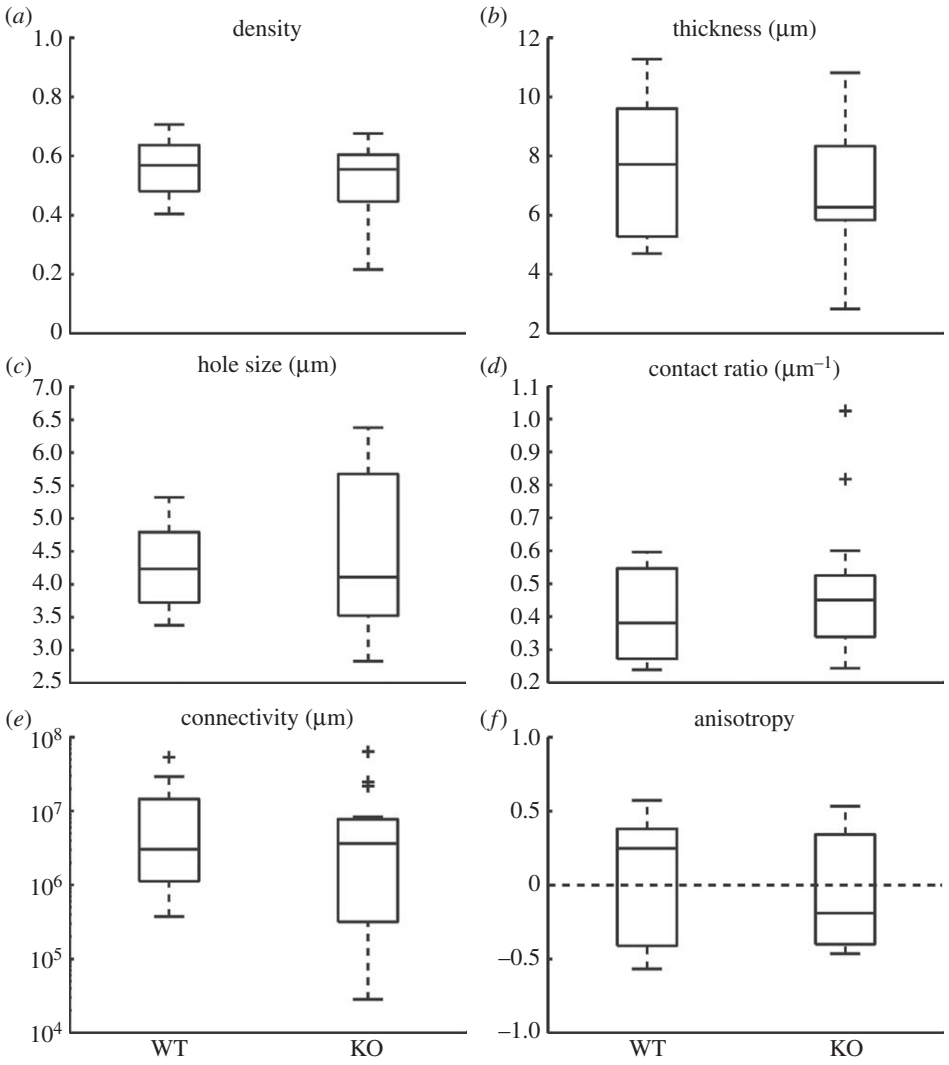

Figure 4. Metric values of ICC networks from *Ano1* dataset. No statistically significant differences ($p < 0.05$) were present. A plus symbol in the boxplot resembles an outlier.

could also serve a functional purpose, to optimize the distribution of electrical activity generated by the remaining ICC. If this remodelling did not occur, an increase in the spacing between ICC processes may lead to insufficient or patchy delivery of current to activate neighbouring SMC regions.

Another interesting and novel result from the analysis of the *5-HT$_{2B}$* ICC-depleted networks was the preferential alignment of ICC processes in the longitudinal direction. The mechanisms for this anisotropic remodelling are uncertain, however, it is possible that it could also convey functional benefits for the ICC-depleted tissue, by retaining the propagation of slow waves down the organ as opposed to around it. If longitudinal coupling of slow waves is disrupted such that the activity is not entrained down the tract, then ICC control over intestinal slow wave frequency plateaus may be impaired or lost [37]. Therefore, during ICC depletion, the ICC network would need to be more intact longitudinally than circularly to deliver consistent entrained activity. Our results of remodelling during ICC depletion await confirmation in other animal models and in disease states before the broader significance of these findings and their meaning can be understood.

The results of comparing the 3-day versus 4-week WT ICC networks give rise to an additional 'pruning' hypothesis that may occur during ICC network maturation. Although the immature networks had the same density as the mature ones, the processes were thinner and more closely spaced. This suggested that the immature networks had a larger number of processes. The lower connectivity of the immature networks may be because of the presence of partially pruned processes, and the increased contact ratio may be due to the thinner processes. A detailed study on the post-natal developments of ICC in the murine small intestine was conducted by Mei *et al.* [38]. Although the quantitative analysis was primarily limited to ICC counts, a thickening of ICC processes during post-natal maturation was also visually observed [38]. An analogous mechanism of synaptic pruning exists in neuroscience, where an initial synaptic overgrowth is followed by judicial pruning during development [39]. This process is thought to serve physiological purposes of reparation and development, and ultimately to maintain efficient brain function [40]. Similarly, the abundance of processes in the immature ICC networks may not all be necessary or efficient, and throughout maturation the redundant or less effective ones would be discarded. As ICC networks only acquire adult morphology in the suckling period [41], pruning may optimize network performance to accommodate for the increasing work load due to organ growth [38] and maturing dietary influences.

The animal models used in this paper do not show any physical changes to the organ size, and hence the changes in network properties identified reflect the structural changes

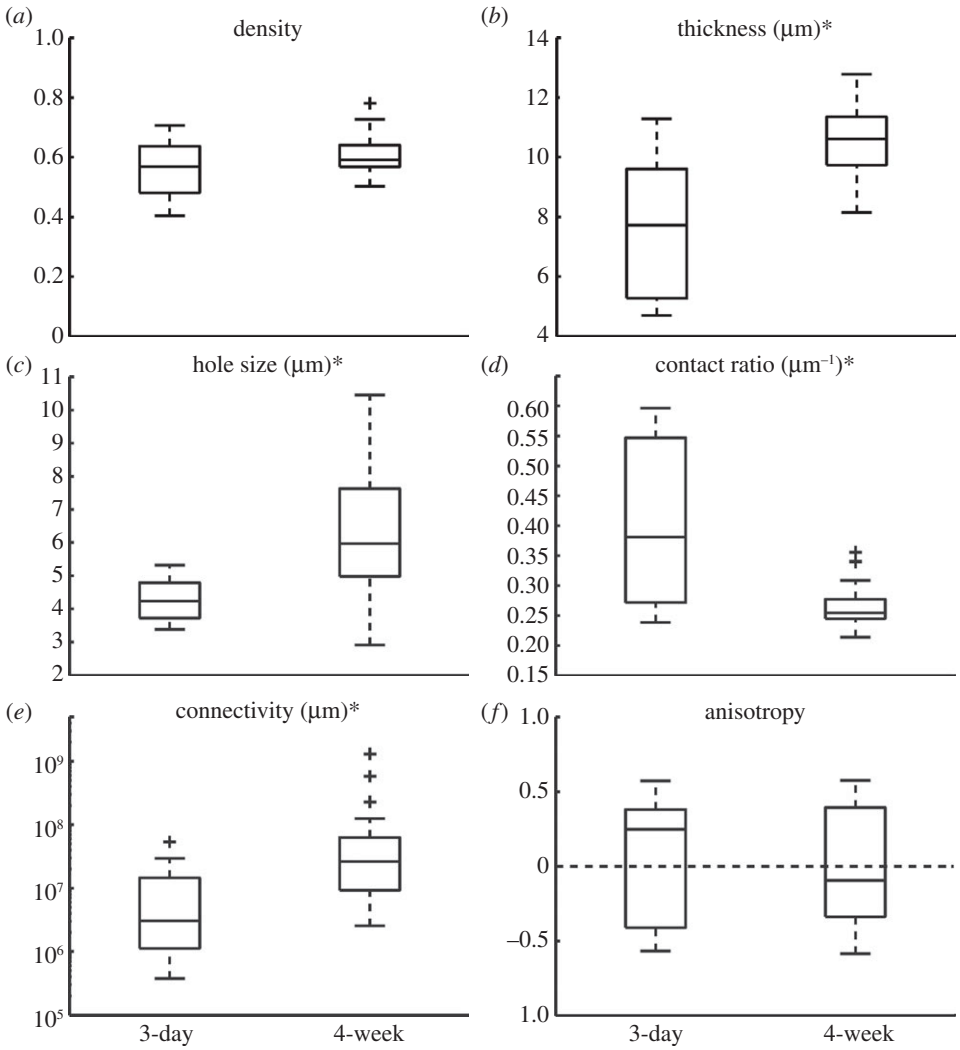

Figure 5. Metric values of 3-day and 4-week WT ICC networks from the *Ano1* and *5-HT$_{2B}$* receptor datasets, respectively. An asterisk in the figure title indicates a statistically significant difference ($p < 0.05$). A plus symbol in the boxplot resembles an outlier.

specifically occurring within the ICC networks, rather than being an epiphenomenon. However, in studies where the organ is likely to exhibit physical changes, such as tissue distension in pseudo-obstruction and similar animal models, additional measures should be taken into account for changes in organ size when applying these metrics on the imaging data. One such strategy, as employed previously [11], is to stain for another unaffected cell type, for example, smooth muscle nuclei as well as for ICC, and then the nuclei counts can be used as a normalizing factor to ensure standardized structural comparison between different tissue samples. On the other hand, stretch induced by tissue handling in the experimental procedure may still be present, and hence may have influenced some of the numerical metric values. It is difficult to differentiate between this stretch effect and natural variation in the ICC network structure, both of which may have contributed to the large variance in the reported results. Although measures for minimizing errors due to stretch have and should be taken (i.e. meticulous care in tissue handling, multiple samples), methods for further addressing this issue need to be investigated.

A limitation of the thickness and hole size metrics is the lack of sensitivity to tapering effects. That is, the thickness metric does not significantly respond to the rate of decrease of thickness along a cell body or process, and the hole size metric does not effectively reflect the rate of decrease of radius within a non-ICC region. In the computation of these

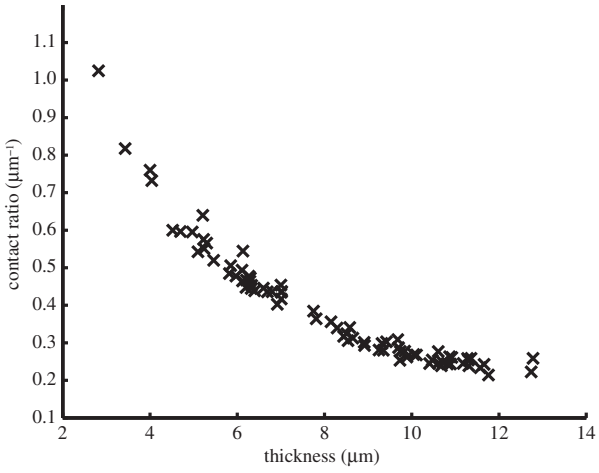

Figure 6. Contact ratio versus thickness metric values of WT and KO networks from both *5-HT$_{2B}$* receptor and *Ano1* datasets.

metrics, only the regional maxima of the distance transforms were taken into account. This efficiently captures the general structures of interest, but may ignore the finer details of the tapering regions. However, even if quantified, tapering effects are not expected to have a large influence on the metric values. Also, as demonstrated in figure 1*f*, ICC islands may be identified falsely under a limited field of view, which influences

Table 1. Potential physiological relevance of the ICC structural metrics in the context of the pacemaker activity generated by ICC-MP.

metric	potential physiological relevance
density	measures the ICC network volume, reflecting the amount of bioelectrical current generated
thickness	measures the width of cellular structures within the ICC network, which may impact electrical activity propagation through the network
hole size	reflects the distribution of ICC throughout the tissue (i.e. the 'tightness' of the network), and may relate to the uniformity of SMC activation
contact ratio	indicates the availability of conduction pathways from ICC to non-ICC regions within the MP, which may (through field coupling conduction mechanism [32]) relate to the efficiency of pacemaker activity conduction into SMC
connectivity	reflects the structural integrity of the ICC network, indicating the cohesion of entrainment pathways [33]
anisotropy	indicates the degree of preferential alignment of ICC structures, and may reflect the dominant slow wave propagation direction, potentially affecting predilection and resilience to dysrhythmia [34]

the connectivity metric value. That is, a single ICC island may be identified as multiple islands as the ICC pathways connecting them is outside the current field of view. To mitigate this potential error, a larger field of view should be used where possible. This would potentially capture the necessary ICC pathways, and even if not, the larger tissue area would lessen the magnitude of the introduced error. In calculating the anisotropy metric, the longitudinal and circular directions of the organ were assumed to be orthogonal. This assumption is expected to be reasonably accurate, but at the same time it is unlikely these directions are exactly perpendicular, and hence minor errors would be introduced into this metric value.

In this study, we have applied only the structural metrics on ICC-MP networks, but in fact the metrics can be applied on any two-dimensional imaging data, including biological network structures from different organs, regions or populations. However, it should be borne in mind that the interpretation of the metric results should always be inferred back to the structures being analyzed. Also, the definitions of the numerical metrics presented are for two-dimensional analysis, but the concepts are readily extendable to three dimensions. This extension is mandatory in order to apply the metrics to human imaging data, as the ICC reside in much thicker tissue volumes [12] with processes extending in the transmural direction as well [42], and hence two-dimensional representations of the network structures become inadequate. The current implementation of the numerical metrics was relatively computationally inexpensive for small ICC networks. However, as large-scale imaging data become available [43] or as the metrics are extended to three dimensions, the computational costs incurred will increase, and hence the implementation may be revised to improve efficiency.

The functional significance of the potential remodelling and pruning phenomena discussed here could be investigated using mathematical simulation techniques, whereby the network structures are coupled to an electrical activity modelling framework and embedded biophysically based cell models, as previously demonstrated in GI tissue-specific modelling studies [20,25]. The simulated slow wave propagation across ICC networks could then be correlated to the structural changes observed in the confocal images.

In summary, this paper presented a set of novel numerical metrics for assessing the structural properties of confocal ICC networks. These metrics allowed for the first detailed automated analyses and unbiased quantitative comparisons of ICC network structures, and their demonstration studies revealed novel network remodelling and pruning phenomena that may be important for ICC function.

Acknowledgements. The authors would like to thank Dr Vivek Tharayil for his assistance with the immunohistochemistry for detecting ICC.

Funding statement. J.G. is supported by a University of Auckland Health Research Doctoral Scholarship, a Freemasons Postgraduate Scholarship, and a R. H. T. Bates Postgraduate Scholarship. This work is funded in part by grants from the New Zealand Health Research Council, and National Institutes of Health grants (DK57061, DK68055 and DK64775).

References

1. Farrugia G. 2008 Interstitial cells of Cajal in health and disease. *Neurogastroenterol. Motil.* **20**(Suppl. 1), 54–63. (doi:10.1111/j.1365-2982.2008.01109.x)
2. Hanani M, Farrugia G, Komuro T. 2005 Intercellular coupling of interstitial cells of Cajal in the digestive tract. *Int. Rev. Cytol.* **242**, 249–282.
3. Lees-Green R, Du P, O'Grady G, Beyder A, Farrugia G, Pullan AJ. 2011 Biophysically based modeling of the interstitial cells of Cajal: current status and future perspectives. *Front. Physiol.* **2**, 29. (doi:10.3389/fphys.2011.00029)
4. Ward SM, Burns AJ, Torihashi S, Sanders KM. 1994 Mutation of the proto-oncogene c-Kit blocks development of interstitial cells and electrical rhythmicity in murine intestine. *J. Physiol.* **480**, 91–97.
5. Huizinga JD, Thuneberg L, Kluppel M, Malysz J, Mikkelsen HB, Bernstein A. 1995 *W/kit* gene required for interstitial cells of Cajal and for intestinal pacemaker activity. *Nature* **373**, 347–349. (doi:10.1038/373347a0)
6. Burns AJ, Lomax AE, Torihashi S, Sanders KM, Ward SM. 1996 Interstitial cells of Cajal mediate inhibitory neurotransmission in the stomach. *Proc. Natl Acad. Sci. USA* **93**, 12 008–12 013. (doi:10.1073/pnas.93.21.12008)
7. Farrugia G, Lei S, Lin X, Miller SM, Nath KA, Ferris CD, Levitt M, Szurszewski JH. 2003 A major role for carbon monoxide as an endogenous hyperpolarizing factor in the gastrointestinal tract. *Proc. Natl Acad. Sci. USA* **100**, 8567–8570. (doi:10.1073/pnas.1431233100)
8. Won KJ, Sanders KM, Ward SM. 2005 Interstitial cells of Cajal mediate mechanosensitive responses in the stomach. *Proc. Natl Acad. Sci. USA* **102**, 14 913–14 918. (doi:10.1073/pnas.0503628102)
9. Strege PR, Ou Y, Sha L, Rich A, Gibbons SJ, Szurszewski JH *et al*. 2003 Sodium current in human intestinal interstitial cells of Cajal.

Am. J. Physiol. Gastrointest. Liver Physiol. **285**, G1111–G1121.

10. Huizinga JD, Zarate N, Farrugia G. 2009 Physiology, injury and recovery of interstitial cells of Cajal: basic and clinical science. *Gastroenterology* **137**, 1548–1556. (doi:10.1053/j.gastro.2009.09.023)
11. O'Grady G *et al*. 2012 Abnormal initiation and conduction of slow-wave activity in gastroparesis, defined by high-resolution electrical mapping. *Gastroenterology* **143**, 589–598e3. (doi:10.1053/j.gastro.2012.05.036)
12. Grover M *et al*. 2011 Cellular changes in diabetic and idiopathic gastroparesis. *Gastroenterology* **140**, 1575–1585. (doi:10.1053/j.gastro.2011.01.046)
13. Lyford GL *et al*. 2002 Pan-colonic decrease in interstitial cells of Cajal in patients with slow transit constipation. *Gut* **51**, 496–501. (doi:10.1136/gut.51.4.496)
14. Wedel T, Spiegler J, Soellner S, Roblick UJ, Schiedeck THK, Bruch HP, Krammer H-J. 2002 Enteric nerves and interstitial cells of Cajal are altered in patients with slow-transit constipation and megacolon. *Gastroenterology* **123**, 1459–1467. (doi:10.1053/gast.2002.36600)
15. Feldstein AE, Miller SM, El-Youssef M, Rodeberg D, Lindor NM, Burgart LJ, Szurszewski JH, Farrugia G. 2003 Chronic intestinal pseudoobstruction associated with altered interstitial cells of Cajal networks. *J. Pediatr. Gastroenterol. Nutr.* **36**, 492–497. (doi:10.1097/00005176-200304000-00016)
16. Isozaki K, Hirota S, Miyagawa J, Taniguchi M, Shinomura Y, Matsuzawa Y. 1997 Deficiency of c-Kit+ cells in patients with a myopathic form of chronic idiopathic intestinal pseudo-obstruction. *Am. J. Gastroenterol.* **92**, 332–334.
17. Gomez-Pinilla PJ *et al*. 2011 Changes in interstitial cells of Cajal with age in the human stomach and colon. *Neurogastroenterol. Motil.* **23**, 36–44. (doi:10.1111/j.1365-2982.2010.01590.x)
18. Burns AJ, Herbert TM, Ward SM, Sanders KM. 1997 Interstitial cells of Cajal in the guinea-pig gastrointestinal tract as revealed by c-Kit immunohistochemistry. *Cell Tissue Res.* **290**, 11–20. (doi:10.1007/s004410050902)
19. Tharayil VS *et al*. 2010 Lack of serotonin 5-HT_{2B} receptor alters proliferation and network volume of interstitial cells of Cajal *in vivo*. *Neurogastroenterol. Motil.* **22**, 462–e110. (doi:10.1111/j.1365-2982.2009.01435.x)
20. Gao J, Du P, Archer R, O'Grady G, Gibbons SJ, Farrugia G, Cheng LK, Pullan AJ. 2011 A stochastic multi-scale model of electrical function in normal and depleted ICC networks. *IEEE Trans. Biomed. Eng.* **58**, 3451–3455. (doi:10.1109/TBME.2011.2164248)
21. Odgaard A. 1997 Three-dimensional methods for quantification of cancellous bone architecture. *Bone* **20**, 315–328. (doi:10.1016/S8756-3282(97)00007-0)
22. Wood EJ. 1990 Applying Fourier and associated transforms to pattern characterization in textiles. *Text Res. J.* **60**, 212–220. (doi:10.1177/004051759006000404)
23. Prim RC. 1957 Shortest connection networks and some generalizations. *Bell Syst. Tech. J.* **36**, 1389–1401.
24. Komuro T. 2006 Structure and organization of interstitial cells of Cajal in the gastrointestinal tract. *J. Physiol.* **576**, 653–658. (doi:10.1113/jphysiol.2006.116624)
25. Du P, O'Grady G, Gibbons SJ, Yassi R, Lees-Green R, Farrugia G, Cheng LK, Pullan AJ. 2010 Tissue-specific mathematical models of slow wave entrainment in wild-type and 5-HT_{2B} knockout mice with altered interstitial cells of Cajal networks. *Biophys. J.* **98**, 1772–1781. (doi:10.1016/j.bpj.2010.01.009)
26. Miller SM, Farrugia G, Schmalz PF, Ermilov LG, Maines MD, Szurszewski JH. 1998 Heme oxygenase 2 is present in interstitial cell networks of the mouse small intestine. *Gastroenterology* **114**, 239–244. (doi:10.1016/S0016-5085(98)70473-1)
27. Wouters M, Gibbons SJ, Roeder JL, Distad M, Ou Y, Strege PR, Szurszewski JH, Farrugia G. 2007 Exogenous serotonin regulates proliferation of interstitial cells of Cajal in mouse jejunum through 5-HT_{2B} receptors. *Gastroenterology* **133**, 897–906. (doi:10.1053/j.gastro.2007.06.017)
28. Gomez-Pinilla PJ *et al*. 2009 Ano1 is a selective marker of interstitial cells of Cajal in the human and mouse gastrointestinal tract. *Am. J. Physiol. Gastrointest. Liver Physiol.* **296**, G1370–G1381. (doi:10.1152/ajpgi.00074.2009)
29. Stanich JE, Gibbons SJ, Eisenman ST, Bardsley MR, Rock JR, Harfe BD, Ordog T, Farrugia G. 2011 Ano1 as a regulator of proliferation. *Am. J. Physiol. Gastrointest. Liver Physiol.* **301**, G1044–G1051. (doi:10.1152/ajpgi.00196.2011)
30. Pearson K. 1901 On lines and planes of closest fit to systems of points in space. *Phil. Mag.* **2**, 559–572.
31. He CL, Soffer EE, Ferris CD, Walsh RM, Szurszewski JH, Farrugia G. 2001 Loss of interstitial cells of Cajal and inhibitory innervation in insulin-dependent diabetes. *Gastroenterology* **121**, 427–434. (doi:10.1053/gast.2001.26264)
32. Huizinga JD, Liu LWC, Blennerhassett MG, Thuneberg L, Molleman A. 1992 Intercellular communication in smooth muscle. *Experientia* **48**, 932–941. (doi:10.1007/BF01919140)
33. van Helden DF, Laver DR, Holdsworth J, Imtiaz MS. 2010 Generation and propagation of gastric slow waves. *Clin. Exp. Pharmacol. Physiol.* **37**, 516–524. (doi:10.1111/j.1440-1681.2009.05331.x)
34. O'Grady G *et al*. 2012 Rapid high-amplitude circumferential slow wave propagation during normal gastric pacemaking and dysrhythmias. *Neurogastroenterol. Motil.* **24**, e299–e312. (doi:10.1111/j.1365-2982.2012.01932.x)
35. Kluppel M, Huizinga J, Malysz J, Bernstein A. 1998 Developmental origin and Kit-dependent development of the interstitial cells of Cajal in the mammalian small intestine. *Dev. Dyn.* **211**, 60–71. (doi:10.1002/(SICI)1097-0177(199801)211:1<60::AID-AJA6>3.0.CO;2-5)
36. Horváth VJ, Vittal H, Lörincz A, Chen H, Almeida-Porada G, Redelman D, Tamas A. 2006 Reduced stem cell factor links smooth myopathy and loss of interstitial cells of Cajal in murine diabetic gastroparesis. *Gastroenterology* **130**, 759–770. (doi:10.1053/j.gastro.2005.12.027)
37. Conklin JL, Du C. 1990 Pathways of slow-wave propagation in proximal colon of cats. *Am. J. Physiol. Gastrointest. Liver Physiol.* **258**, G894–G903.
38. Mei F *et al*. 2009 An age-dependent proliferation is involved in the postnatal development of interstitial cells of Cajal in the small intestine of mice. *Histochem. Cell Biol.* **131**, 43–53. (doi:10.1007/s00418-008-0515-7)
39. Chechik G, Meilijson I, Ruppin E. 1998 Synaptic pruning in development: a computational account. *Neural Comput.* **10**, 1759–1777. (doi:10.1162/089976698300017124)
40. Chechik G, Meilijson I, Ruppin E. 1999 Neuronal regulation: a mechanism for synaptic pruning during brain maturation. *Neural Comput.* **11**, 2061–2080. (doi:10.1162/089976699300016089)
41. Faussone-Pellegrini MS, Matini P, Stach W. 1996 Differentiation of enteric plexuses and interstitial cells of Cajal in the rat gut during pre- and postnatal life. *Acta Anat.* **155**, 113–125. (doi:10.1159/000147796)
42. Liu YA, Chung YC, Pan ST, Hou YC, Peng SJ, Pasricha PJ, Tang S-C. 2012 3-D illustration of network orientations of interstitial cells of Cajal subgroups in human colon as revealed by deep-tissue imaging with optical clearing. *Am. J. Physiol. Gastrointest. Liver Physiol.* **302**, G1099–G1110. (doi:10.1152/ajpgi.00432.2011)
43. Sands GB, Gerneke DA, Hooks DA, Green CR, Smaill BH, Legrice IJ. 2005 Automated imaging of extended tissue volumes using confocal microscopy. *Microsc. Res. Techniq.* **67**, 227–239. (doi:10.1002/jemt.20200)